Materials Today Physics 54 (2025) 101721

Contents lists available at ScienceDirect

Materials Today Physics

journal homepage: www.journals.elsevier.com/materials-today-physics

Electronic and phononic characteristics of high-performance radiative cooling pigments h-BN: A comparative study to $BaSO_4$

Ziqi Guo[1], Ioanna Katsamba[1], Daniel Carne, Dudong Feng, Kellan Moss, Emily Barber, Ziqi Fang, Andrea Felicelli, Xiulin Ruan *

School of Mechanical Engineering and the Birck Nanotechnology Center, Purdue University, West Lafayette, 47907, IN, USA

ARTICLE INFO

Keywords:
Phonon scattering
Radiative cooling
h-BN
First-principles calculation
Photon Monte Carlo simulations

ABSTRACT

A thin layer, lightweight, and ultra-white hexagonal boron nitride (h-BN) nanoporous paint has been developed recently. However, the underlying atomic and nanostructural physics of the paint's radiative cooling performance remains quite elusive. In this work, a multiscale, multiphysics computational framework is employed to gain atomic level insights of the high radiative cooling performance. By leveraging first-principles calculations to study the electronic transitions and phonon dynamics, the refractive index and extinction coefficient are predicted across solar and mid-infrared (mid-IR) spectra, which are then used to calculate the optical properties of a single nanoparticle either by Mie Theory or computationally solving Maxwell's Equations. Subsequently, the photon Monte Carlo simulation is used to predict the photon transport in nanoplatelet-matrix nanocomposites, by including the anisotropic optical properties of nanoplatelets for the first time. The predicted solar reflectance and sky window emissivity of the nanocomposites agree well with the experiments. By comparing with $BaSO_4$-based paint, we attribute the high solar reflectance of h-BN paint at a lower thickness to its higher refractive index and nanoplatelet morphology, and attribute the relatively lower sky window emissivity to its lower extinction coefficient in mid-IR. Surprisingly, aligning the nanoplatelets horizontally does not significantly improve the solar reflectance at 150 μm coating thickness due to diminishing returns. Finally, we compile many radiative cooling pigments and order the following few in decreasing refractive index: h-BN, $BaSO_4$, $CaCO_3$, SiO_2. Our work advances the understanding of atomic-scale features in designing radiative cooling materials.

1. Introduction

Radiative cooling, an innovative passive cooling technology, has attracted substantial research interest in recent years. By reflecting solar irradiation to avoid solar heating and dissipating heat into cold deep space through the sky window (8-13 μm), radiative cooling can significantly reduce energy consumption and mitigate climate change. It has been used for various of applications including space cooling [1], building cooling [2], energy harvesting [3], agriculture [4], and personal thermal management [5].

The pursuit of effective radiative cooling materials is of great research interest. The ideal materials should possess a combination of high reflectance in the solar spectrum (0.25-2.5 μm) and high emissivity in the sky window region. The foundation can be traced back to the 20th century [6], where full daytime below-ambient cooling was achieved with dual-layer structures (TiO_2/PVF nanocomposite on the aluminum substrate). However, this early success was limited since solar reflectance was significantly boosted by the metal substrate rather than the paint itself. Over decades, this field has witnessed remarkable evolution driven by advancements in materials science, optics, and nanotechnology. Daytime radiative cooling has been achieved by using the multilayer structure [7], metal–dielectric photonic structure [8], porous polymer [9], glass-polymer hybrid metamaterial [10], and delignified wood [11]. However, these approaches rely on complicated structures and pose challenges for real-world applications.

Radiative cooling paint, which can be applied using standard brush, roller, or spray-painting techniques, offers a desirable advantage over other types of materials since it is easy to scale and apply to real-world surfaces, including non-flat and irregularly shaped ones. It is also a sustainable and cost-effective cooling solution for both residential and commercial applications. Recently, daytime radiative cooling has been achieved by ultra-white paints based on calcium carbonate ($CaCO_3$) [12], barium sulfate ($BaSO_4$) [13] and hexagonal boron nitride

* Corresponding author.
E-mail address: ruan@purdue.edu (X. Ruan).
[1] These authors contributed equally to this work.

https://doi.org/10.1016/j.mtphys.2025.101721
Received 17 January 2025; Received in revised form 24 March 2025; Accepted 6 April 2025
Available online 20 April 2025

(h-BN) [14] nanoparticles, which have exceptional solar reflectance and high emittance in the sky window. Specifically, the h-BN-acrylic paint achieves solar reflectance of 97.9%, and sky window emissivity of 0.83 with only 150 μm thickness, which enables 5-6 °C below ambient cooling on average. The high solar reflectance and mid-IR emissivity suggest potential applications in building cooling, where passive cooling coatings on rooftops substantially reduce air conditioning energy consumption and mitigate the global warming effect. Additionally, the lightweight and high-performance characteristics of h-BN-based paint make it particularly suitable for wearable devices, aerospace and automotive applications, where reducing weight while maintaining thermal regulation is critical. h-BN nanoparticle has also been used as fillers in various applications, such as photonic films [15–17], aerogels [18], and fabrics [19], to enhance radiative cooling performance.

However, the underlying atomic level physics of h-BN-based paint's extraordinary performance, especially the sky window emissivity, is not fully understood. A comparison with $BaSO_4$-based counterparts [13] reveals intriguing differences. While $BaSO_4$ paints show a solar reflectance of 98.1%, h-BN paints achieve similar solar reflectance with a significantly thinner coating (400 μm vs. 150 μm). Although previous work [14] has studied its high solar reflectance with the photon Monte Carlo simulation, the angle dependency due to platelet-shape particles and the anisotropic properties of h-BN was not considered. Additionally, the high anisotropic refractive index of h-BN requires further investigation at the atomic level. Moreover, $BaSO_4$-acrylic paint shows a higher sky-window emittance compared to h-BN (0.95 vs. 0.83), yet the mechanisms behind this phenomenon remain unclear. Furthermore, as the pursuit of these efficient radiative cooling paints is based on a trial-and-error method, the atomic and structural characteristics are crucial for designing high-performance radiative cooling materials. Answering these questions requires multiscale multiphysics insights. The optical properties of bulk materials, particularly their refractive index (n) and extinction coefficient (κ), have a high impact on the radiative cooling performance. These properties arise from intricate interactions between photons, electrons, and phonons, which are investigated by atomic scale simulations such as first-principles calculation [20–25]. Additionally, at subwavelength scales, strong light–matter interactions come into play, where factors such as pigment size, shape, and morphology have a substantial impact, which follows the principles of Maxwell's equations. Studying the different physical mechanisms at these different scales is required to understand h-BN's unique radiative cooling properties.

In this work, we present a multiscale multiphysics framework to predict the radiative cooling performance of h-BN-based paint. At the atomic scale, we use first-principles calculations to predict the refractive index and extinction coefficient, including solving electronic transition and phonon scattering. At the microscale, we model photon scattering and absorption of individual nanoplatelets using Finite Element Method (FEM) simulations for solar regions and Mie Theory for mid-IR regions, accounting for their anisotropic shape and optical properties. Finally, at the macroscale, we employ a Monte Carlo photon transport model to simulate radiative transfer within the nanocomposite, predicting solar reflectance and mid-infrared emissivity. This integrated approach allows us to bridge atomic-scale material properties with real-world optical performance, and to involve multiphysics including photons, electrons, and phonons, offering more insights into radiative cooling paint. Compared to prior studies, our work incorporates the anisotropic optical properties of the nanoplatelets, enabling a more accurate description of light scattering and absorption characteristics in h-BN-based paints for the first time. Our simulation agrees well with the experimental results. By comparing h-BN with $BaSO_4$-acrylic paint [26], we found several atomic and structural characteristics: (1) h-BN has a higher refractive index and a band gap higher than the highest solar photon energy, which enhances solar scattering and eliminates solar absorption. (2) Aligning the nanoplatelets to horizontal orientations would increase but does not significantly improve the solar reflectance. (3) Due to the lack of IR-active phonon modes, h-BN has a lower extinction coefficient in the sky window, which results in a lower sky window emissivity. Our computational framework and the identified material characteristics provide valuable tools and insights for advancing the development of radiative cooling paint.

2. Method and simulation details

We start from conducting first-principles predictions to obtain the optical constants, including refractive index and extinction coefficient, of h-BN. All the Density-functional theory (DFT) calculations were conducted using Vienna Ab initio Simulation Package (VASP) [27]. The dielectric function in the solar spectrum is determined by the electronic transition mechanism. Given the limitation of DFT calculations in accurately predicting band gaps, we applied the GW correction [28] to refine our results. This significantly improved the accuracy of our electronic structure predictions by considering quasiparticle energies and incorporating electron–electron interactions beyond the scope of DFT. We then calculated the optical properties of h-BN by solving the Bethe–Salpeter Equation (BSE) [29] on top of the GW-corrected result, which allowed us to accurately capture the excitonic effects.

In the mid-IR region, the dielectric response could be obtained by solving phonon dynamics, which includes calculating a set of harmonic and anharmonic interatomic force constants (IFCs) and calculating phonon scattering. The 2nd-IFC and phonon dispersion was obtained from density functional perturbation theory (DFPT) [30] calculation using Phonopy [31]. The 3rd- and 4th-IFCs were calculated using the Finite Difference Method (FDM) using Thirdorder.py [32] and Fourthorder.py [33] packages. The three-phonon (3ph) and four-phonon (4ph) scattering calculations were performed using the Sheng-BTE [32] package integrated with the FourPhonon module [33] based on the relaxation time approximation (RTA). A sampling-based approach [34] was adopted to accelerate the 4ph scattering calculation. The overall phonon scattering rate was calculated based on spectral Matthiessen's rule [35]: $\tau_\lambda^{-1} = (\tau_\lambda^{3ph})^{-1} + (\tau_\lambda^{4ph})^{-1} + (\tau_\lambda^{iso})^{-1}$, where $(\tau_\lambda^{3ph})^{-1}$, $(\tau_\lambda^{4ph})^{-1}$ and $(\tau_\lambda^{iso})^{-1}$ are 3ph, 4ph and isotope scattering rate, respectively. The phonon linewidth, measured in cm^{-1}, is proportional to the scattering rate of zone-center optical phonons as $2\pi c\gamma_\lambda = \tau_\lambda^{-1}$. The dielectric response in the mid-IR region was calculated using a four-parameter Lorentz oscillator model [36–38]:

$$\varepsilon(\omega) = \varepsilon_\infty \prod_m \left(\frac{\omega_{LO,m}^2 - \omega^2 - i\gamma_{LO,m}\omega}{\omega_{TO,m}^2 - \omega^2 - i\gamma_{TO,m}\omega} \right) \quad (1)$$

where ε_∞ is the high-frequency dielectric constant obtained by the DFPT calculation, ω is the photon frequency, m goes over all the IR-active TO phonon modes, $\omega_{TO,m}$ and $\omega_{LO,m}$ are resonance frequencies of the IR-active TO and the paired LO phonon modes, respectively, and $\gamma_{TO,m}$ and $\gamma_{LO,m}$ are the corresponding damping factors. The n and κ can be derived from the dielectric function: $\varepsilon = (n + i\kappa)^2$. More simulation details can be found in Supplementary Materials Section 1.

Following the first-principles predictions of the dielectric function, we predicted the spectral optical response of the h-BN-based nanocomposite. Directly solving the Maxwell equations is highly computational expensive. Instead, we assume the paints are continuous mediums with effective properties [39] to simulate the photon transport within the paint layer. Initially, the scattering and absorption coefficients, as well as the asymmetry parameter of a single nanoparticle, are calculated. Then, the photon Monte Carlo simulation is used to predict the nanocomposite's reflectance, transmittance, and emittance. In the solar spectrum, given that the photon wavelength is comparable to the particle size, the particle morphology and orientation would significantly influence the optical properties. Therefore, a 3D FEM simulation was conducted on a single h-BN nanoplatelet to obtain the optical properties under different orientations. We focus on three particular particle orientations, including horizontal, random, and vertical (details

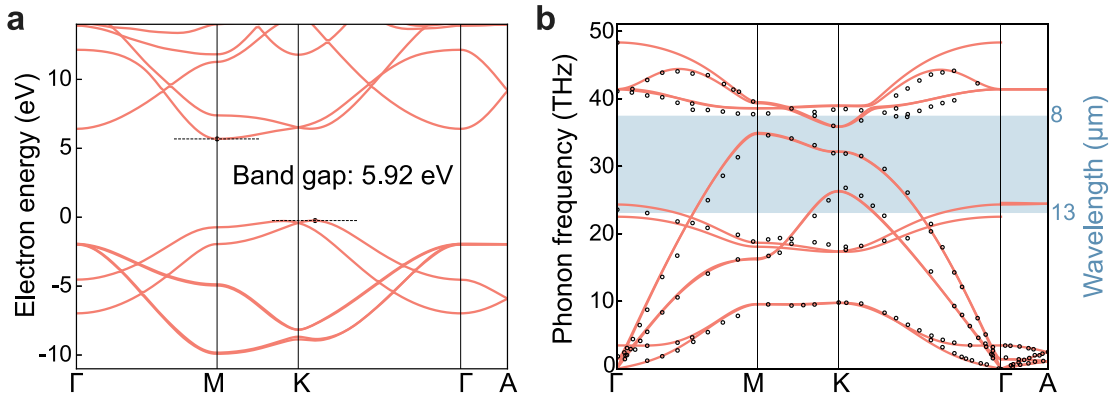

Fig. 1. First-principles predicted electronic band structure and phonon dispersion of h-BN. a, Electronic band structure, **b,** Phonon dispersion. The blue-shaded region represents the wavelength range of the sky window. The black dots are experimental results from Ref. [41].

in Supplementary Materials Section 2 and 3). As for the mid-IR region, where the particle size is much smaller than the wavelength, the scattering becomes weak, and the discrepancy brought by the morphology does not affect the properties we are interested in. Therefore, we use the Mie theory to solve for the input coefficients for higher computational efficiency. The comparison with FEM simulations is provided in the Supplementary Materials Section 4. More details on the photon Monte Carlo simulation are provided in Supplementary Materials Section 5.

The total solar reflectance R_s is calculated by:

$$R_s = \frac{\int_{\lambda_1}^{\lambda_2} R_\lambda \, G_\lambda \, d\lambda}{\int_{\lambda_1}^{\lambda_2} G_\lambda \, d\lambda} \tag{2}$$

where λ is the photon wavelength, R_λ is the spectral reflectance and G_λ is the spectral solar irradiation. The integration is conducted between 0.28 μm and 2.5 μm.

The sky window emissivity ε_{sky} is calculated by:

$$\varepsilon_{sky} = \frac{\int_{\lambda_1}^{\lambda_2} \varepsilon_\lambda \, E_b(\lambda, T) \, d\lambda}{\int_{\lambda_1}^{\lambda_2} E_b(\lambda, T) \, d\lambda} \tag{3}$$

where ε_λ is the spectral emissivity and $E_b(\lambda, T)$ is the black body radiation from a surface at room temperature. The integration is conducted between 8 μm and 13 μm.

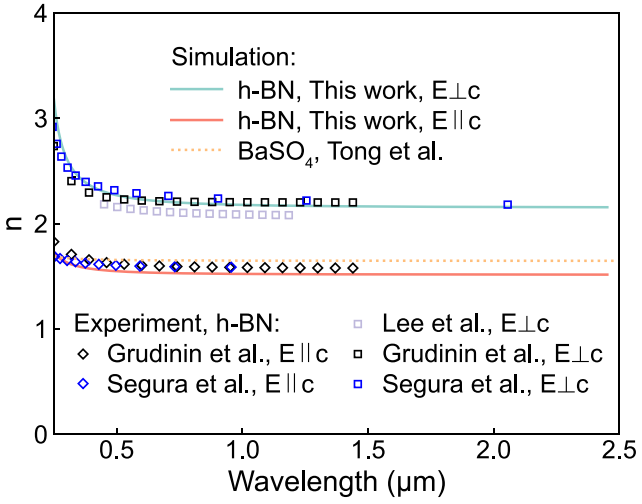

Fig. 2. Refractive index of h-BN in the UV–VIS-NIR region. The in-plane and out-of-plane n of h-BN are shown as green and red lines, respectively. Experimental data from Grudinin et al. [42] (black), Segura et al. [43] (dark blue) and Lee et al. [44] (gray) are provided for comparison. The in-plane and out-of-plane experimental data are shown as diamond and square dots, respectively. The n of $BaSO_4$ [26] is provided for comparison.

3. Results

3.1. Electronic band structure and phonon dispersion

The predicted electronic band structure, as shown in Fig. 1a, indicates that h-BN is an indirect band gap material with a 5.92 eV band gap. The band gap agrees with experimental data reported by Cassabois et al. [40] (5.955 eV). Notably, the band gap of h-BN exceeds the highest photon energy in the solar spectrum (4.13 eV), which would result in negligible solar absorption. Fig. 1b shows the phonon dispersion of h-BN, which has a good agreement with experiment [41]. Note that the zone-center optical phonon modes fall nearly outside of the sky window region, which influences the dielectric response and will be discussed later.

3.2. Refractive index prediction from first-principles

The predicted refractive index of h-BN in the UV–VIS-NIR region is shown in Fig. 2, demonstrating a good agreement with the experimental data [42–44]. Additionally, we include the optical properties of $BaSO_4$ for comparison and find the in-plane (E ∥ c-axis) n of h-BN is higher than $BaSO_4$ in the solar spectrum. Our observation follows the established inverse relationship between the optical refractive index and the material's band gap [45], as the band gap of $BaSO_4$ (7.6 eV [46]) is higher than that of h-BN. The high n of h-BN is beneficial for enhancing photon scattering, which is favored in improving solar reflectance. Additionally, it was noted that the in-plane n of h-BN is higher than the out-of-plane (E ⊥ c-axis) value, attributed to the stronger polarizability arising from strong intralayer covalent bonds compared to weaker interlayer Van der Waals forces. This also makes it beneficial to orient the nanoplatelets perpendicular to the incident sunlight direction (horizontal orientation in the later paragraph), which would lead to a stronger scattering of sunlight.

In the mid-IR spectrum, the calculated n and κ also match the experimental results [42–44], as shown in Fig. 3. Notably, in the sky window region, the κ value is much smaller than $BaSO_4$. This is attributed to the frequency, damping factor, and oscillator strength of phonon resonances in both materials (see the exact values in Supplementary Materials Section 6). For h-BN, the two IR-active phonon modes have small damping and large LO–TO splitting, which lead to strong resonances and high peaks in κ. However, since neither of these modes falls between 8-13 μm, the κ remains small within the sky window. On the other hand, $BaSO_4$ has multiple phonon modes within the sky window, with high damping factors and low oscillator strength. This leads to a

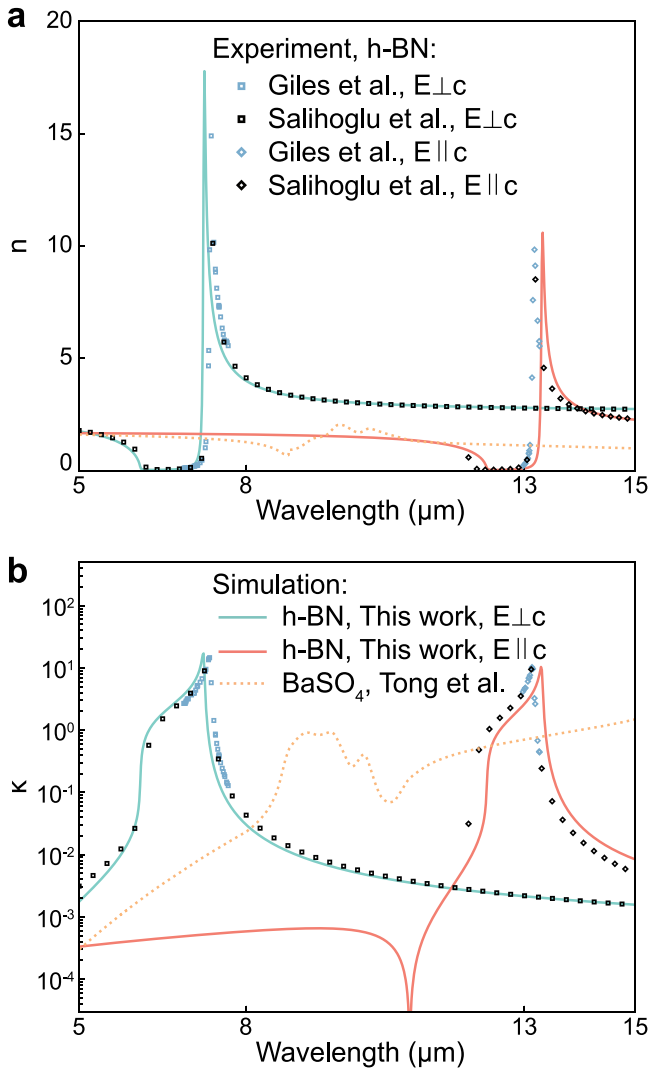

Fig. 3. Refractive index of h-BN in the mid-IR region. The n and κ in in-plane and out-of-plane directions are shown as green and red lines, respectively. Experimental data from Giles et al. [47] (blue) and Salihoglu et al. [48] (black) are provided for comparison. The in-plane and out-of-plane experimental data are shown as diamond and square dots, respectively. The simulated n and κ of $BaSO_4$ [26] are presented for comparison.

higher κ than h-BN in the sky window which enhances absorption. We also studied the contribution of phonon renormalization on h-BN and found it to be negligible, as demonstrated in Supplementary Materials Section 7.

3.3. Spectral optical response of nanocomposites from photon Monte Carlo simulation

Next, we use the Monte Carlo method to predict the spectral optical response of the nanocomposite, as illustrated in Fig. 4. For the solar spectrum, the predicted solar reflectance of h-BN-acrylic nanocomposite with random particle orientations is 96.4%, which agrees well with the experimental result (97.9%). The small discrepancy is due to the air voids found in the nanocomposite, which are not included in this model. A comparably high solar reflectance between h-BN and $BaSO_4$-acrylic nanocomposite (96.4% vs. 98.1%) was observed, while h-BN achieves such performance with a much thinner thickness (150 μm vs. 400 μm) due to its higher n value enhanced scattering.

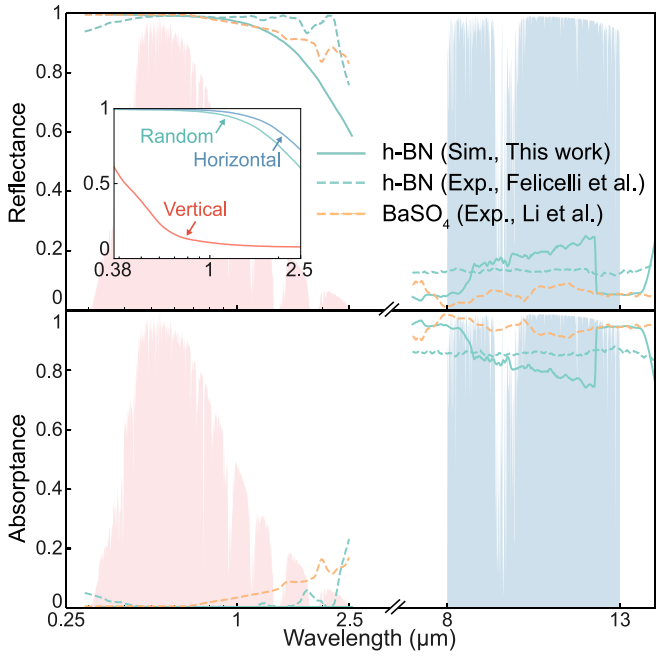

Fig. 4. Reflectance and absorptance of h-BN-acrylic nanocomposite. The experimental results from Ref. [14] and our simulations are shown in dash and solid lines, respectively. The scaled AM1.5 solar spectrum [49] (pink shaded area) and the clear sky atmospheric transmittance in the mid-IR region [50] (blue shaded area) are plotted for reference. The experimental data for $BaSO_4$ is from Ref. [13] and is plotted for comparison. In the subfigure, we compare the solar reflectance of random particle orientation with cases where nanoplatelets are placed parallel and perpendicular to the paint upper surface, named horizontal and vertical in legend, respectively.

We also studied the effect of the orientation of h-BN nanoplatelets, as shown in the subfigure of Fig. 4. The solar reflectance reaches the maximum when all the particles are oriented horizontally. When the particles are randomly oriented, the solar reflectance slightly decreases but remains largely unaffected. In contrast, the reflectance drops significantly when the particles are fully oriented vertically. This behavior can be attributed to the angular-dependent optical properties of individual particles, as shown in Fig. 5. Since the horizontal orientation has both the highest scattering coefficient and the highest asymmetry parameter, it has the largest backscattering effect, while the vertical orientation has the least backscattering. However, due to the saturation of scattering effects, making the nanoplatelets more horizontally aligned yields diminishing returns. As the scattering coefficient rises, the incremental gain in reflectance decreases (see Supplementary Section 8). Since the scattering coefficient at random orientations is quite high already, additional horizontal alignment does not significantly enhance reflectance, as most incident photons are already scattered effectively. This explains why the solar reflectance of the horizontal orientation shows only marginal improvement over the random case. It implies that even if not all the particles are oriented in the optimal way, h-BN nanoplatelets can achieve high reflectance. Our conclusion holds particularly true for nanocomposites with high h-BN concentrations and sufficient thickness. In weight-sensitive applications requiring thinner coatings, optimal particle orientation can still enhance reflectance by up to 10% (see Supplementary Materials Section 9).

In the mid-IR region, our simulation shows a sky window emissivity of 0.84, closely matching the experimental result in Ref. [14] (0.83). The discrepancy in the spectral emissivity could stem from the defect and impurities in the h-BN nanoplatelet and neglecting the air pores, which would further enhance the scattering and increase the absorption. Note that since the infrared measurement of h-BN-acrylic paint was performed on a reflective aluminum substrate to

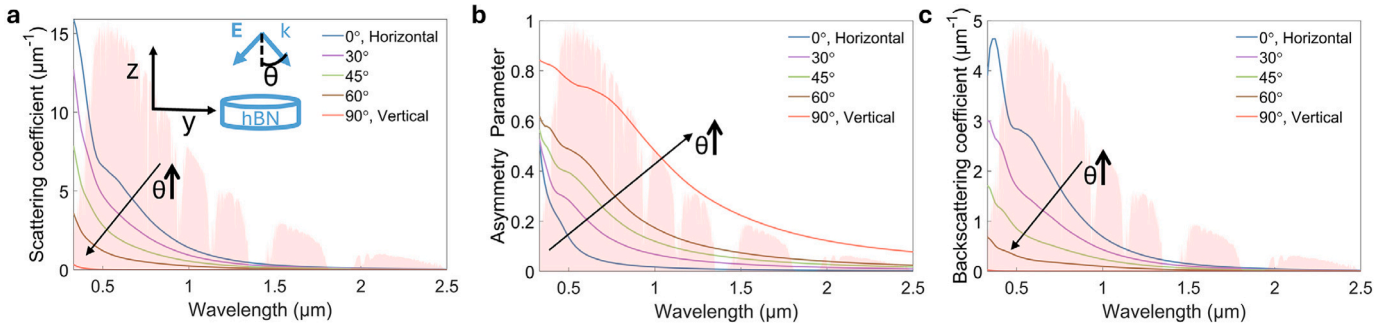

Fig. 5. Results via FEM model for multiple angle orientation. a, The scattering coefficient decreases with an increase in angle. **b**, The asymmetry parameter increases with an increase in the angle. For platelets vertically orientated, the asymmetry parameter is close to the expected one for spherical particles. **c**, The backscattering coefficient decreases with an increase in angle.

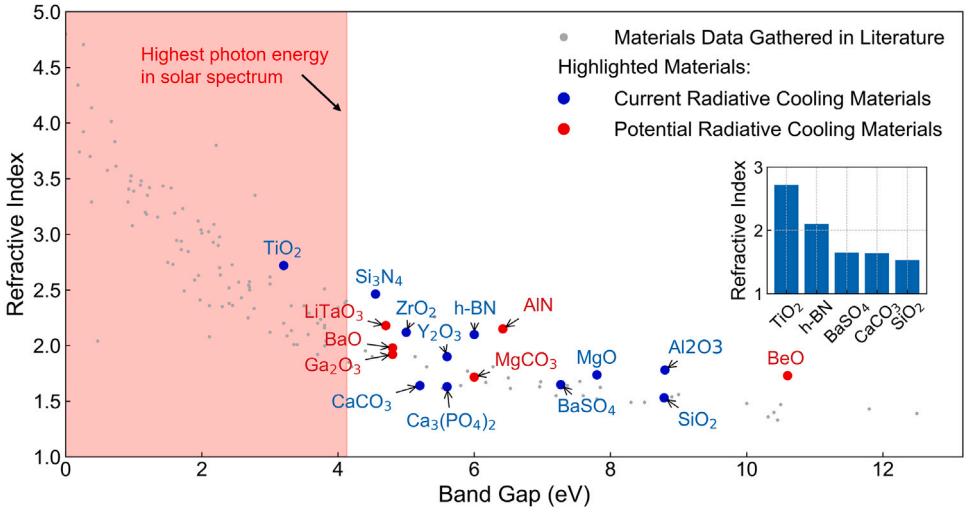

Fig. 6. Relation between optical refractive index and band gap. The gray dots show the inverse trend between the refractive index and the band gap of materials. Data are gathered from Ref. [51–74]. The blue dots show several radiative cooling materials that has been studied in Ref. [6,12–14,68,75–81]. The red dots show potential radiative cooling materials with high band gap and high refractive index. The subplot compares the refractive index of several common radiative cooling materials.

avoid any undesired overestimation of the emissivity due to absorption by the substrate, our simulations assumed the bottom layer to be aluminum for simulations in the mid-IR region. The emissivity values we reported should be considered as a lower bound of the actual performance when painted onto real-world surfaces. When compared to $BaSO_4$-based paint, the sky window emissivity of h-BN-based paint is considerably lower (0.83 versus 0.95). This is due to a lower κ value and a lower thickness of h-BN-based paint, which leads to more photons exiting the nanocomposite without being absorbed. In contrast, once the photon comes into the medium of $BaSO_4$-based paint, they are unlikely to leave due to higher κ and higher thickness.

4. Discussion

Based on the comparative study between h-BN and $BaSO_4$, we gain some insights into the atomic and structural characteristics of high-performance radiative cooling paint pigment. High solar reflectance is essential for radiative cooling applications. In radiative cooling paint, solar reflectance primarily relies on photon scattering, which is enhanced by the large impedance between the nanoparticles and the surrounding matrix. Therefore, a high refractive index of the nanoparticle material can significantly enhance the solar reflectance. Besides, to minimize solar absorption, a material with a band gap exceeding 4.13 eV—corresponding to the highest photon energy in the solar spectrum—is desirable. Many radiative cooling materials reported in literature follow these rules, as shown in Fig. 6a. However, increasing the band gap would typically reduce the refractive index [45]. Therefore, identifying materials with both high n and a large band gap is crucial in the discovery of potential radiative cooling materials. Based on this rule, we manually search and identify several potential radiative cooling materials for future investigations, as shown in Fig. 6b. High-throughput screening and machine learning for material property discovery would greatly accelerate this process, as shown in recent works [82–86]. Apart from the material properties, we found that aligning the nanoplatelet horizontally would also help enhance the scattering and improve the solar reflectance. However, the effect can be small compared to random orientations, especially with high concentrations and sufficient thicknesses such as 150 μm. In addition, factors such as the nanoparticle sizes and distribution [87] also play an important role in solar reflectance. Regarding the emissivity, a high sky window emissivity is favored to maximize the cooling power. A high value of κ would increase the absorption of paint. Achieving such properties typically requires materials with multiple IR-active phonon modes with large damping in the sky window. Further work on high-throughput screening of phonon dispersion and scattering is important to find high-emissivity materials.

While our multiscale multiphysics framework provides valuable insights, there are a few limitations to our work. The neglect of air pores within the nanocomposite may introduce discrepancies between predicted and experimental results, as air pores can influence additional

scattering. Additionally, although the assumption of an effective scattering medium with homogeneous optical properties has been demonstrated to agree with experiments, a direct Monte Carlo simulation tracking the exact positions of scatterers could provide better accuracy.

5. Conclusion

In conclusion, our work employs a multiscale multiphysics simulation approach to predict the radiative cooling performance of h-BN-based nanocomposites. Starting from h-BN atomic structures, we conduct electronic transition and phonon dynamics calculations to predict the dielectric response of h-BN in the solar spectrum and mid-IR regions. We then calculated the optical properties of a single h-BN anisotropic nanoplatelet, including the angular dependency in the solar region for the first time. Incorporating the photon Monte Carlo calculation enables us to evaluate the solar reflectance and sky window emissivity of h-BN-based nanocomposites. The predictions are in good agreement with the experiment. We further highlight key characteristics in the design of high-performance radiative cooling materials. Our computational framework is a useful approach for the future development of efficient radiative cooling paint, contributing to significant energy savings and carbon footprint reduction and supporting global sustainability efforts.

CRediT authorship contribution statement

Ziqi Guo: Writing – review & editing, Writing – original draft, Visualization, Validation, Software, Resources, Methodology, Investigation, Formal analysis, Data curation, Conceptualization. **Ioanna Katsamba:** Writing – review & editing, Writing – original draft, Visualization, Validation, Methodology, Investigation, Formal analysis, Data curation. **Daniel Carne:** Writing – review & editing, Software, Methodology. **Dudong Feng:** Writing – review & editing, Investigation. **Kellan Moss:** Writing – review & editing, Visualization, Data curation. **Emily Barber:** Writing – review & editing, Data curation. **Ziqi Fang:** Writing – review & editing, Data curation. **Andrea Felicelli:** Writing – review & editing, Data curation. **Xiulin Ruan:** Writing – review & editing, Supervision, Project administration, Methodology, Investigation, Funding acquisition, Formal analysis, Conceptualization.

Declaration of competing interest

The authors declare the following financial interests/personal relationships which may be considered as potential competing interests: Ziqi Guo, Ioanna Katsamba, Dudong Feng, Daniel Carne reports financial support was provided by National Science Foundation. If there are other authors, they declare that they have no known competing financial interests or personal relationships that could have appeared to influence the work reported in this paper.

Acknowledgments

Z.G., I.K., D.F., D.C., and X.R. acknowledge partial support from US National Science Foundation through Award #2102645. Z.G is partly supported by the System Fellows 2024 Doctoral Fellowship provided by the Purdue Systems Collaboratory at Purdue University. A.F. and E.B. acknowledge support from the US National Science Foundation through a Graduate Research Fellowship.

Appendix A. Supplementary data

Supplementary material related to this article can be found online at https://doi.org/10.1016/j.mtphys.2025.101721.

Data availability

Data will be made available on request.

References

[1] M. Holynska, Y. Butenko, R. Martins, C. Semprimoschnig, F. Meyer, S. Faber, Studies of white ceramic coatings for esa's BepiColombo mission to mercury, J. Spacecr. Rockets 56 (5) (2019) 1358–1370.
[2] J. Peoples, Y.-W. Hung, Z. Fang, J. Braun, W.T. Horton, X. Ruan, Energy savings of radiative cooling paints applied to residential buildings, Int. J. Heat Mass Transfer 194 (2022) 123001.
[3] A.P. Raman, W. Li, S. Fan, Generating light from darkness, Joule 3 (11) (2019) 2679–2686.
[4] C.-H. Liu, C. Ay, J.-C. Kan, M.-T. Lee, The effect of radiative cooling on reducing the temperature of greenhouses, Materials 11 (7) (2018) 1166.
[5] M.I. Iqbal, K. Lin, F. Sun, S. Chen, A. Pan, H.H. Lee, C.-W. Kan, C.S.K. Lin, C.Y. Tso, Radiative cooling nanofabric for personal thermal management, ACS Appl. Mater. & Interfaces 14 (20) (2022) 23577–23587.
[6] A. Harrison, M. Walton, Radiative cooling of TiO2 white paint, Sol. Energy 20 (2) (1978) 185–188.
[7] A.P. Raman, M.A. Anoma, L. Zhu, E. Rephaeli, S. Fan, Passive radiative cooling below ambient air temperature under direct sunlight, Nature 515 (7528) (2014) 540–544.
[8] E. Rephaeli, A. Raman, S. Fan, Ultrabroadband photonic structures to achieve high-performance daytime radiative cooling, Nano Lett. 13 (4) (2013) 1457–1461.
[9] J. Mandal, Y. Fu, A.C. Overvig, M. Jia, K. Sun, N.N. Shi, H. Zhou, X. Xiao, N. Yu, Y. Yang, Hierarchically porous polymer coatings for highly efficient passive daytime radiative cooling, Science 362 (6412) (2018) 315–319.
[10] Y. Zhai, Y. Ma, S.N. David, D. Zhao, R. Lou, G. Tan, R. Yang, X. Yin, Scalable-manufactured randomized glass-polymer hybrid metamaterial for daytime radiative cooling, Science 355 (6329) (2017) 1062–1066.
[11] T. Li, Y. Zhai, S. He, W. Gan, Z. Wei, M. Heidarinejad, D. Dalgo, R. Mi, X. Zhao, J. Song, et al., A radiative cooling structural material, Science 364 (6442) (2019) 760–763.
[12] X. Li, J. Peoples, Z. Huang, Z. Zhao, J. Qiu, X. Ruan, Full daytime sub-ambient radiative cooling in commercial-like paints with high figure of merit, Cell Rep. Phys. Sci. 1 (10) (2020).
[13] X. Li, J. Peoples, P. Yao, X. Ruan, Ultrawhite BaSO4 paints and films for remarkable daytime subambient radiative cooling, ACS Appl. Mater. & Interfaces 13 (18) (2021) 21733–21739.
[14] A. Felicelli, I. Katsamba, F. Barrios, Y. Zhang, Z. Guo, J. Peoples, G. Chiu, X. Ruan, Thin layer lightweight and ultrawhite hexagonal boron nitride nanoporous paints for daytime radiative cooling, Cell Rep. Phys. Sci. 3 (10) (2022).
[15] P. Li, A. Wang, J. Fan, Q. Kang, P. Jiang, H. Bao, X. Huang, Thermo-optically designed scalable photonic films with high thermal conductivity for subambient and above-ambient radiative cooling, Adv. Funct. Mater. 32 (5) (2022) 2109542.
[16] X.-Y. Xu, H. Zhang, X.-J. Kang, Y.-Z. Zhang, C.-Y. He, X.-H. Gao, High-performance, superhydrophobic, durable photonic structure coating for efficient passive daytime radiative cooling, Mater. Today Phys. 48 (2024) 101556.
[17] H. Fu, Y. Zhang, X. Liu, H. Han, H. Kondo, H. Zhou, Flexible highly thermal conductive hybrid film for efficient radiative cooling, Sol. Energy Mater. Sol. Cells 266 (2024) 112660.
[18] W. Cai, Z. Li, H. Xie, W. Wang, T. Cui, B. Lin, L. Qi, X. Hu, Y. Du, Y. Ming, et al., Thermally managed and fireproof composite aerogels for safer and year-round energy saving, Chem. Eng. J. 483 (2024) 149006.
[19] X. Zhang, T. Zhang, Y. Cao, Y. Jiang, Y. Chen, Y. Li, D. Yu, W. Wang, A janus infrared emission dual-mode super-fabric for sustainable efficient thermal management, Chem. Eng. J. 503 (2025) 158664.
[20] X. Yang, T. Feng, J.S. Kang, Y. Hu, J. Li, X. Ruan, Observation of strong higher-order lattice anharmonicity in Raman and infrared spectra, Phys. Rev. B 101 (16) (2020) 161202.
[21] R. Asahi, Y. Taga, W. Mannstadt, A.J. Freeman, Electronic and optical properties of anatase TiO 2, Phys. Rev. B 61 (11) (2000) 7459.
[22] R. Saniz, L.-H. Ye, T. Shishidou, A. Freeman, Structural, electronic, and optical properties of NiAl 3: first-principles calculations, Phys. Rev. B 74 (1) (2006) 014209.
[23] Z. Guo, Z. Han, A. Alkandari, K. Khot, X. Ruan, First-principles prediction of thermal conductivity of bulk hexagonal boron nitride, Appl. Phys. Lett. 124 (16) (2024).
[24] Z. Guo, P. Sokalski, Z. Han, Y. Cheng, L. Shi, T. Taniguchi, K. Watanabe, X. Ruan, First-principles prediction of zone-center optical phonon linewidths and IR spectra of hexagonal boron nitride, Appl. Phys. Lett. 125 (23) (2024) 231106.
[25] A. Alkandari, Z. Han, Z. Guo, T.E. Beechem, X. Ruan, Anisotropic anharmonicity dictates the thermal conductivity of β-Ga 2 O 3, Physical Review B 111 (9) (2025) 094308.

[26] Z. Tong, J. Peoples, X. Li, X. Yang, H. Bao, X. Ruan, Electronic and phononic origins of BaSO4 as an ultra-efficient radiative cooling paint pigment, Mater. Today Phys. 24 (2022) 100658.
[27] G. Kresse, J. Furthmüller, Efficient iterative schemes for ab initio total-energy calculations using a plane-wave basis set, Phys. Rev. B 54 (16) (1996) 11169.
[28] M. Shishkin, G. Kresse, Implementation and performance of the frequency-dependent GW method within the PAW framework, Phys. Rev. B— Condens. Matter Mater. Phys. 74 (3) (2006) 035101.
[29] S. Albrecht, L. Reining, R. Del Sole, G. Onida, Ab initio calculation of excitonic effects in the optical spectra of semiconductors, Phys. Rev. Lett. 80 (20) (1998) 4510.
[30] S. Baroni, S. De Gironcoli, A. Dal Corso, P. Giannozzi, Phonons and related crystal properties from density-functional perturbation theory, Rev. Modern Phys. 73 (2) (2001) 515.
[31] A. Togo, I. Tanaka, First principles phonon calculations in materials science, Scr. Mater. 108 (2015) 1–5.
[32] W. Li, J. Carrete, N.A. Katcho, N. Mingo, Shengbte: A solver of the Boltzmann transport equation for phonons, Comput. Phys. Comm. 185 (6) (2014) 1747–1758.
[33] Z. Han, X. Yang, W. Li, T. Feng, X. Ruan, FourPhonon: An extension module to shengbte for computing four-phonon scattering rates and thermal conductivity, Comput. Phys. Comm. 270 (2022) 108179.
[34] Z. Guo, Z. Han, D. Feng, G. Lin, X. Ruan, Sampling-accelerated prediction of phonon scattering rates for converged thermal conductivity and radiative properties, Npj Comput. Mater. 10 (1) (2024) 31.
[35] J. Ziman, Electrons and Phonons: The Theory of Transport Phenomena in Solids, Oxford University Press, Northamptonshire, 2001.
[36] M. Born, K. Huang, M. Lax, Dynamical theory of crystal lattices, Am. J. Phys. 23 (7) (1955) 474.
[37] A. Barker Jr., Transverse and longitudinal optic mode study in MgF2 and ZnF2, Phys. Rev. 136 (5A) (1964) A1290.
[38] F. Gervais, B. Piriou, Anharmonicity in several-polar-mode crystals: adjusting phonon self-energy of LO and TO modes in al2o3 and TiO2 to fit infrared reflectivity, J. Phys. C: Solid State Phys. 7 (13) (1974) 2374.
[39] D. Carne, J. Peoples, Z. Guo, D. Feng, Z. Han, X. Liu, X. Ruan, FOS: A fully integrated open-source program for fast optical spectrum calculations of nanoparticle media, Comput. Phys. Comm. (2024) 109393.
[40] G. Cassabois, P. Valvin, B. Gil, Hexagonal boron nitride is an indirect bandgap semiconductor, Nat. Photonics 10 (4) (2016) 262–266.
[41] J. Serrano, A. Bosak, R. Arenal, M. Krisch, K. Watanabe, T. Taniguchi, H. Kanda, A. Rubio, L. Wirtz, Vibrational properties of hexagonal boron nitride: inelastic X-ray scattering and ab initio calculations, Phys. Rev. Lett. 98 (9) (2007) 095503.
[42] D. Grudinin, G. Ermolaev, D. Baranov, A. Toksumakov, K. Voronin, A. Slavich, A. Vyshnevyy, A. Mazitov, I. Kruglov, D. Ghazaryan, et al., Hexagonal boron nitride nanophotonics: a record-breaking material for the ultraviolet and visible spectral ranges, Mater. Horizons 10 (7) (2023) 2427–2435.
[43] A. Segura, L. Artús, R. Cuscó, T. Taniguchi, G. Cassabois, B. Gil, Natural optical anisotropy of h-BN: Highest giant birefringence in a bulk crystal through the mid-infrared to ultraviolet range, Phys. Rev. Mater. 2 (2) (2018) 024001.
[44] S.-Y. Lee, T.-Y. Jeong, S. Jung, K.-J. Yee, Refractive index dispersion of hexagonal boron nitride in the visible and near-infrared, Phys. Status Solidi (B) 256 (6) (2019) 1800417.
[45] T. Moss, Relations between the refractive index and energy gap of semiconductors, Phys. Status Solidi (B) 131 (2) (1985) 415–427.
[46] A. Amiryan, A. Gurvieh, R. Katomina, I.Y. Petrova, N. Soshchin, M. Tombak, Recombination processes and emission spectrum of terbium in oxysulfides, J. Appl. Spectrosc. 27 (3) (1977) 1159–1162.
[47] A.J. Giles, S. Dai, I. Vurgaftman, T. Hoffman, S. Liu, L. Lindsay, C.T. Ellis, N. Assefa, I. Chatzakis, T.L. Reinecke, et al., Ultralow-loss polaritons in isotopically pure boron nitride, Nat. Mater. 17 (2) (2018) 134–139.
[48] H. Salihoglu, V. Iyer, T. Taniguchi, K. Watanabe, P.D. Ye, X. Xu, Energy transport by radiation in hyperbolic material comparable to conduction, Adv. Funct. Mater. 30 (6) (2020) 1905830.
[49] A. Standard, G159, standard tables for references solar spectral irradiance at air mass 1.5: Direct normal and hemispherical for a 37 tilted surface, in: Society for Testing Matls, West Conshocken, PA, USA, 1998.
[50] S.D. Lord, A New Software Tool for Computing Earth's Atmospheric Transmission of Near-And Far-Infrared Radiation, vol. 103957, Ames Research Center, 1992.
[51] P. Hervé, L. Vandamme, General relation between refractive index and energy gap in semiconductors, Infrared Phys. Technol. 35 (4) (1994) 609–615.
[52] A. Lamichhane, Energy-gap-refractive index relations in semiconductors—Using Wemple–DiDomenico model to unify moss, ravindra, and Herve–Vandamme relationships, Solids 4 (4) (2023) 316–326.
[53] H.M. Gomaa, I. Yahia, H. Zahran, Novel empirical correlation between the optical refractive index and energy bandgap in semiconductors: Comparative study, 2021.
[54] V. Dimitrov, S. Sakka, Linear and nonlinear optical properties of simple oxides. II, J. Appl. Phys. 79 (3) (1996) 1741–1745.
[55] S. Tripathy, Refractive indices of semiconductors from energy gaps, Opt. Mater. 46 (2015) 240–246.
[56] H.M. Gomaa, I. Yahia, H. Zahran, Correlation between the static refractive index and the optical bandgap: Review and new empirical approach, Phys. B 620 (2021) 413246.
[57] M. Rubat du Merac, Transparent ceramics: Materials, processing, properties and applications, in: M. Pomeroy (Ed.), Encyclopedia of Materials: Technical Ceramics and Glasses, Elsevier, Oxford, 2021, pp. 399–423.
[58] D. Roessler, W. Walker, E. Loh, Electronic spectrum of crystalline beryllium oxide, J. Phys. Chem. Solids 30 (1) (1969) 157–167.
[59] R. Ropp, Chapter 5 - group 14 (c, si, ge, sn, and pb) alkaline earth compounds, in: R. Ropp (Ed.), Encyclopedia of the Alkaline Earth Compounds, Elsevier, Amsterdam, 2013, pp. 351–480.
[60] F.M. Hossain, B. Dlugogorski, E. Kennedy, I. Belova, G.E. Murch, Electronic, optical and bonding properties of MgCO3, Solid State Commun. 150 (17–18) (2010) 848–851.
[61] I. Bhaumik, R. Bhatt, S. Ganesamoorthy, A. Saxena, A. Karnal, P. Gupta, A. Sinha, S. Deb, Temperature-dependent index of refraction of monoclinic Ga 2 o 3 single crystal, Appl. Opt. 50 (31) (2011) 6006–6010.
[62] M. Mohamed, I. Unger, C. Janowitz, R. Manzke, Z. Galazka, R. Uecker, R. Fornari, The surface band structure of β-Ga2O3, in: Journal of Physics: Conference Series, 286, (1) IOP Publishing, 2011, 012027.
[63] J. Kischkat, S. Peters, B. Gruska, M. Semtsiv, M. Chashnikova, M. Klinkmüller, O. Fedosenko, S. Machulik, A. Aleksandrova, G. Monastyrskyi, et al., Mid-infrared optical properties of thin films of aluminum oxide, titanium dioxide, silicon dioxide, aluminum nitride, and silicon nitride, Appl. Opt. 51 (28) (2012) 6789–6798.
[64] J. Resende, D. Fuard, D. Le Cunff, J.-H. Tortai, B. Pelissier, Hybridization of ellipsometry and energy loss spectra from XPS for bandgap and optical constants determination in SiON thin films, Mater. Chem. Phys. 259 (2021) 124000.
[65] J. Pastrňák, L. Roskovcová, Refraction index measurements on AlN single crystals, Phys. Status Solidi (B) 14 (1) (1966) K5–K8.
[66] X. Fu, Aluminum nitride wide band-gap semiconductor and its basic characteristics, in: 6th International Conference on Electronic, Mechanical, Information and Management Society, Atlantis Press, 2016, pp. 555–558.
[67] D.R. Lide, CRC handbook of chemistry and physics, vol. 85, CRC Press, 2004.
[68] J. Lv, Z. Chen, X. Li, Calcium phosphate paints for full-daytime subambient radiative cooling, ACS Appl. Energy Mater. 5 (4) (2022) 4117–4124.
[69] R.E. Stephens, I.H. Malitson, Index of refraction of magnesium oxide, J. Res. Natl. Bur. Stand. 49 (4) (1952) 249–252.
[70] N.F. Chayed, N. Badar, R. Rusdi, N. Kamarudin, N. Kamarulzaman, Optical band gap energies of magnesium oxide (MgO) thin film and spherical nanostructures, in: AIP Conference Proceedings, 1400, (1) American Institute of Physics, 2011, pp. 328–332.
[71] Y. Nigara, Measurement of the optical constants of yttrium oxide, Japan. J. Appl. Phys. 7 (4) (1968) 404.
[72] W.C. Wang, M. Badylevich, V. Afanas'Ev, A. Stesmans, C. Adelmann, S. Van Elshocht, J. Kittl, M. Lukosius, C. Walczyk, C. Wenger, Band alignment and electron traps in Y2o3 layers on (100) si, Appl. Phys. Lett. 95 (13) (2009).
[73] G. Ghosh, Dispersion-equation coefficients for the refractive index and birefringence of calcite and quartz crystals, Opt. Commun. 163 (1–3) (1999) 95–102.
[74] S. Mohammed, F. Mohammad, J. Sahariya, H. Mund, K. Bhamu, B. Ahuja, Electronic structure of CaCO3: A compton scattering study, Appl. Radiat. Isot. 72 (2013) 64–67.
[75] Y. Zhang, X. Tan, G. Qi, X. Yang, D. Hu, P. Fyffe, X. Chen, Effective radiative cooling with ZrO2/PDMS reflective coating, Sol. Energy Mater. Sol. Cells 229 (2021) 111129.
[76] P. Das, S. Rudra, K.C. Maurya, B. Saha, Ultra-emissive MgO-PVDF polymer nanocomposite paint for passive daytime radiative cooling, Adv. Mater. Technol. 8 (24) (2023) 2301174.
[77] H. Tang, S. Li, Y. Zhang, Y. Na, C. Sun, D. Zhao, J. Liu, Z. Zhou, Radiative cooling performance and life-cycle assessment of a scalable MgO paint for building applications, J. Clean. Prod. 380 (2022) 135035.
[78] Y. Sun, H. He, X. Huang, Z. Guo, Superhydrophobic SiO2–glass bubbles composite coating for stable and highly efficient daytime radiative cooling, ACS Appl. Mater. & Interfaces 15 (3) (2023) 4799–4813.
[79] W. Wei, Y. Zhu, Q. Li, Z. Cheng, Y. Yao, Q. Zhao, P. Zhang, X. Liu, Z. Chen, F. Xu, et al., An Al2O3-cellulose acetate-coated textile for human body cooling, Sol. Energy Mater. Sol. Cells 211 (2020) 110525.
[80] C.-L. Luo, L.-X. Zheng, J.-Y. Jiao, W.-G. Yan, J. Zhao, G.-Z. Jia, Z.-F. Liu, Z.-B. Liu, J.-G. Tian, Enhanced passive radiative cooling coating with Y2O3 for thermal management of building, Opt. Mater. 138 (2023) 113710.
[81] J. Zhao, Q. Meng, Y. Li, Z. Yang, J. Li, Structural porous ceramic for efficient daytime subambient radiative cooling, ACS Appl. Mater. & Interfaces 15 (40) (2023) 47286–47293.
[82] M. Lee, Y. Youn, K. Yim, S. Han, High-throughput ab initio calculations on dielectric constant and band gap of non-oxide dielectrics, Sci. Rep. 8 (1) (2018) 14794.
[83] F. Naccarato, F. Ricci, J. Suntivich, G. Hautier, L. Wirtz, G.-M. Rignanese, Searching for materials with high refractive index and wide band gap: A first-principles high-throughput study, Phys. Rev. Mater. 3 (4) (2019) 044602.

[84] I. Petousis, D. Mrdjenovich, E. Ballouz, M. Liu, D. Winston, W. Chen, T. Graf, T.D. Schladt, K.A. Persson, F.B. Prinz, High-throughput screening of inorganic compounds for the discovery of novel dielectric and optical materials, Sci. Data 4 (1) (2017) 1–12.

[85] A.C. Rajan, A. Mishra, S. Satsangi, R. Vaish, H. Mizuseki, K.-R. Lee, A.K. Singh, Machine-learning-assisted accurate band gap predictions of functionalized mxene, Chem. Mater. 30 (12) (2018) 4031–4038.

[86] Z. Guo, P. Roy Chowdhury, Z. Han, Y. Sun, D. Feng, G. Lin, X. Ruan, Fast and accurate machine learning prediction of phonon scattering rates and lattice thermal conductivity, Npj Comput. Mater. 9 (1) (2023) 95.

[87] D. Carne, J. Peoples, F. Arentz, X. Ruan, True benefits of multiple nanoparticle sizes in radiative cooling paints identified with machine learning, Int. J. Heat Mass Transfer 222 (2024) 125209.